

ResDiff: Combining CNN and Diffusion Model for Image Super-Resolution

Shuyao Shang
Shandong University
202000800098@mail.sdu.edu.cn

Zhengyang Shan
Shandong University
202000800128@mail.sdu.edu.cn

Guangxing Liu
Shandong University
202000800141@mail.sdu.edu.cn

Jinglin Zhang*
Shandong University
jinglin.zhang@sdu.edu.cn

Abstract

*Adapting the Diffusion Probabilistic Model (DPM) for direct image super-resolution is wasteful, given that a simple Convolutional Neural Network (CNN) can recover the main low-frequency content. Therefore, we present **ResDiff**, a novel Diffusion Probabilistic Model based on Residual structure for Single Image Super-Resolution (SISR). ResDiff utilizes a combination of a CNN, which restores primary low-frequency components, and a DPM, which predicts the residual between the ground-truth image and the CNN-predicted image. In contrast to the common diffusion-based methods that directly use LR images to guide the noise towards HR space, ResDiff utilizes the CNN's initial prediction to direct the noise towards the residual space between HR space and CNN-predicted space, which not only accelerates the generation process but also acquires superior sample quality. Additionally, a frequency-domain-based loss function for CNN is introduced to facilitate its restoration, and a frequency-domain guided diffusion is designed for DPM on behalf of predicting high-frequency details. The extensive experiments on multiple benchmark datasets demonstrate that ResDiff outperforms previous diffusion-based methods in terms of shorter model convergence time, superior generation quality, and more diverse samples.*

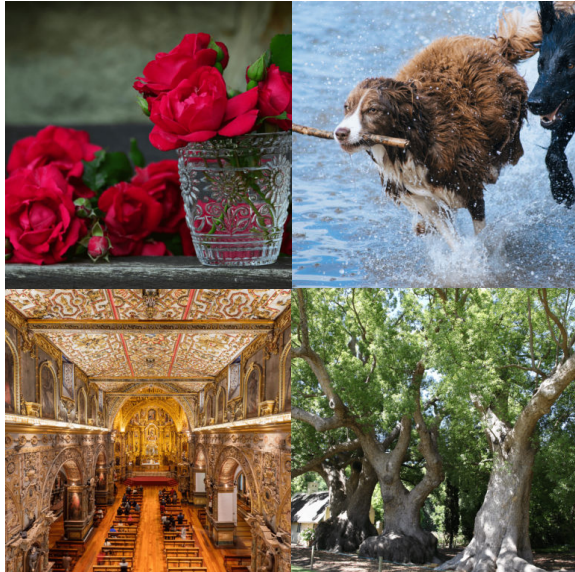
1. Introduction

Single Image Super-Resolution (SISR) is a difficult task in computer vision, which aims to recover high-resolution (HR) images from their low-resolution (LR) counterparts. During image degradation, the high-frequency components are lost, and multiple HR images could produce the same LR image, making this task ill-posed. After Generative Adversarial Networks(GAN) [13] was proposed, the main

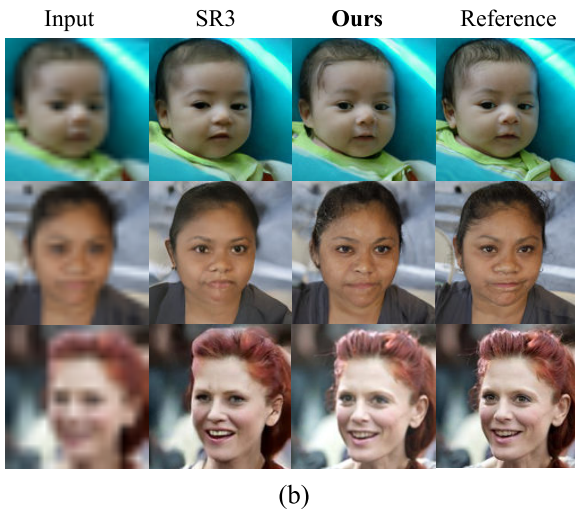
generative-model-based SISR methods are GAN-driven. However, GAN-based methods are hard to train and prone to fall into pattern collapse, causing a lack of diversity. Therefore, a superior generative model is required in the SISR task.

Diffusion Probabilistic Model (DPM) has already demonstrated impressive capabilities in image synthesis [37, 38, 35, 34] and image restoration [6, 22, 45]. It has also shown promising prospects in SISR tasks [39, 25]. However, current Diffusion-based methods for SISR, such as SR3[39], generate HR images directly from random noise, and LR images are only used as conditional input to the diffusion process (Fig.3 (a)). Consequently, the diffusion model needs to recover both the high and low-frequency contents of the image, which not only prolongs the convergence time but also inhibits the model from focusing on the fine-grained information, potentially missing texture details. Li et al.[25] had taken this into account but employed only a bilinear interpolation for the initial prediction, which, compared to CNN, failed to restore sufficiently low-frequency contents and was incapable of generating any high-frequency components in the initial prediction (Fig.3 (b)). Similarly, whang et al.[47] designed a random-sampler and a deterministic-predictor to tackle this problem. However, there is no information interaction between the random-sampler and the deterministic-predictor, resulting in the latter not functioning to its full potential (Fig.3 (c)).

Inspired by the above [25, 47], we propose ResDiff, a residual-structure-based diffusion model. Unlike [25], ResDiff utilizes a CNN for initial prediction. And in contrast to [47], the CNN in ResDiff is pre-trained, thus capable of restoring the major low-frequency components and partial high-frequency components. The initial prediction of the CNN is adopted to guide the random noise towards the Res



(a)



(b)

Figure 1: **Subplot a:** Generated high-resolution samples by our ResDiff ($512 \times 512 \rightarrow 2048 \times 2048$). **Subplot b:** Face super-resolution test results ($4\times$). Compared to SR3, ResDiff generates superior texture details, such as the baby’s eyelids in the first row and the woman’s eyemazing in the third row.

Space (i.e., the residual space between the Ground Truth image and the CNN predicted image). Compared to the methods that only use LR space as guidance, ResDiff can leverage additional information and generate richer high-frequency details. (Fig.3 (d)). Fig.2 presents the structure of ResDiff. The CNN used in ResDiff contains a limited number of parameters. Thus, two more loss functions are introduced to strengthen its recovery capabilities. To further enhance the generation quality, we design a Frequency

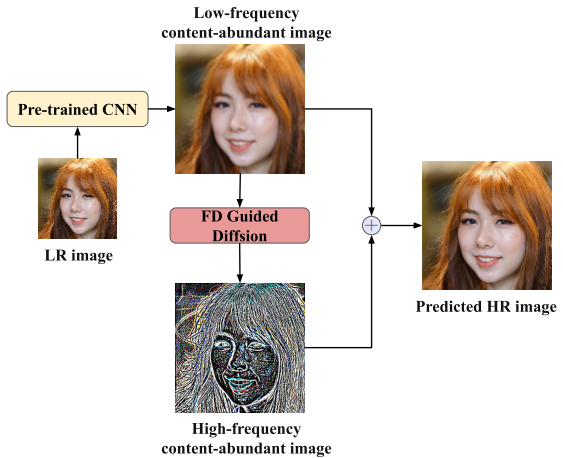


Figure 2: Overall structure of proposed ResDiff.

Domain-guided Diffusion (FD-guided Diffusion) as shown in Fig.3 (d) where the high-frequency space also guides the generation process. FD-guided Diffusion consists of two novel modules. The first is a Frequency-Domain Information Splitter (FD Info Splitter) that separates high-frequency and low-frequency contents and performs adaptive denoising on the noisy image. The second is a high-frequency guided cross-attention module (HF-guided CA) that helps the diffusion model predict high-frequency details.

Experiments on two face datasets (FFHQ and CelebA) and two general datasets (Div2k and Urban100) demonstrate that ResDiff not only accelerates the model’s convergence speed but also generates more fine-grained images, as shown in Fig.1. To verify the generalization of our method, more experiments on different types of datasets are given in the supplementary material.

Our contributions can be summarized as follows:

- **Shorter Convergence Time:** We have designed ResDiff, a residual structure-based diffusion model for the SISR task that leads to an apparent improvement in convergence speed compared to other diffusion-based methods.
- **Superior Generation Quality:** We have introduced FD-guided Diffusion to enhance the diffusion model’s concentration on high-frequency details, resulting in superior generation quality.
- **More Diverse Output:** Experiments have demonstrated that ResDiff holds a lower perceptual-based evaluation value, indicating our method is capable of producing diverse samples.

2. Related Works

Generative-model-based methods have created great success in SISR, which can be classified into GAN-based[24, 44, 32, 43, 50], flow-based[28, 26], and diffusion-based[39, 25] methods.

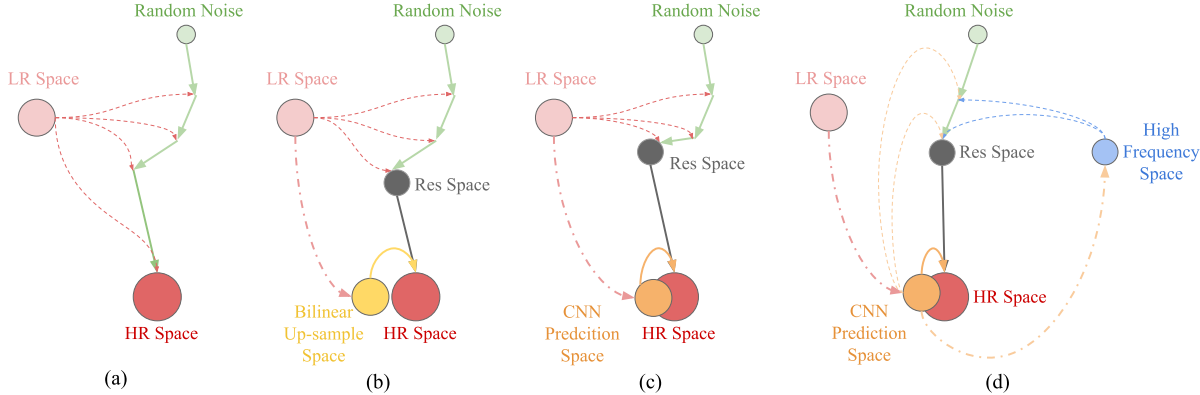


Figure 3: Comparison of different generation processes. In contrast to (a) [39], (b) [25], (c) [47] where only LR Space is used to guide the generation, our ResDiff (d) makes full utilization of CNN Prediction Space and High-Frequency Space to guide a faster and better generation.

GAN-based methods Ledig et al.[24] proposed SRGAN, which employs a perceptual loss function to generate high-quality images. Similarly, Kim et al.[44] introduced ESRGAN, which adopted an enhanced super-resolution GAN and a superior loss function to improve the perceptual quality. GAN-based methods combine content losses with adversarial losses, allowing them to generate sharp edges and richer textures. However, they are prone to mode-collapse, which decreases diversity in the generated SR samples. Moreover, training GANs is challenging and may lead to unexpected artifacts in the generated image.

Flow-based methods Lugmayr et al.[28] proposed SR-Flow, which is a flow-based method that learns the conditional distribution of high-resolution images given their low-resolution counterparts, enabling high-quality image super-resolution with natural and diverse outputs. Flow-based methods map HR images to flow-space latents using an invertible encoder and connect the encoder and decoder with an invertible flow module, which avoids training instability but requires higher training costs and provides lower perceptual quality.

Diffusion-based methods Li et al.[25] introduced SrDiff, the first diffusion-based model for SISR, demonstrating that using the diffusion model for SISR tasks is feasible and promising. Saharia et al. proposed Sr3 [39], which adapts Denoising Diffusion Probabilistic Models (DDPM) to perform SISR tasks, yielding a competitive perceptual-based evaluation value. Diffusion-based methods utilize a diffusion process that simulates noise reduction, resulting in sharper and more detailed images. However, a high computational cost is needed due to multiple forward and backward passes through the entire network during the training process. Our proposed ResDiff, though without improving the training speed of a single iteration, accelerates conver-

gence, which can alleviate this issue from another perspective.

3. Denosing Diffusion Probabilistic Models

The diffusion model, first proposed by Sohl-Dickstein et al.[41] and developed by Ho et al.[16], is a generative model that leverages the diffusion process to model the data distribution. A denoising diffusion probabilistic model (DDPM) employs two Markov chains. One is a forward chain that adds gaussian noise to data:

$$q(x_t|x_{t-1}) = \mathcal{N}(x_t; \sqrt{1 - \beta_t}x_{t-1}, \beta_t I) \quad (1)$$

where $\beta_t \in (0, 1)$ for all $t = 1, \dots, T$ and is a pre-chosen hyperparameter.

Using the reparameterization trick, we can obtain x_t directly from x_0 :

$$q(x_t|x_0) = \mathcal{N}(x_t; \sqrt{\bar{\alpha}_t}x_0, (1 - \bar{\alpha}_t)I) \quad (2)$$

where $\alpha_t = 1 - \beta_t$ and $\bar{\alpha}_t = \prod_{i=0}^t \alpha_i$.

The other Markov chain is a reverse chain that converts noise back into data distribution:

$$p_\theta(x_{t-1}|x_t) = \mathcal{N}(x_{t-1}; \mu_\theta(x_t, t), \Sigma_\theta(x_t, t)) \quad (3)$$

where θ denotes model parameters, and the mean or variance is parameterized by this model.

The forward chain aims to convert any data distribution into a standard Gaussian distribution. In contrast, the reverse Markov chain employs a neural network, such as a U-net[36], to learn transition kernels that reverse the effects of the forward chain. To generate new data, a random variable x_T is initially sampled from the standard Gaussian distribution, followed by ancestral sampling via the reverse Markov chain.

Algorithm 1 ResDiff Inference

Input: low-resolution image x_{LR} ; pre-trained CNN; μ_θ and Σ_θ in Eq.3;
Output: High-resolution image generated by ResDiff;
1: $x_{cnn} = \text{CNN}(x_{LR})$
2: $x_T \sim \mathcal{N}(0, I)$
3: **for** $t = T : 1$ **do**
4: $\epsilon \sim \mathcal{N}(0, I)$ if $t > 1$, else $\epsilon = 0$
5: $x_{t-1} = \mu_\theta(x_t, t, x_{cnn}) + \sqrt{\Sigma_\theta(x_t, t, x_{cnn})} \epsilon$
6: **end for**
7: **return** $x_0 + x_{cnn}$

To optimize the model, we choose to maximize the variational lower bound (VLB). According to [16, 39, 47], the loss function can be written as:

$$\min_{\theta} L(\theta) = \mathbb{E}[\|\epsilon - \epsilon_\theta(x_t, t)\|_1] \quad (4)$$

where ϵ is a randomly generated gaussian noise, ϵ_θ is our noise predictor network, and $x_t = \sqrt{\bar{\alpha}_t}x_0 + (1 - \bar{\alpha}_t)\epsilon$.

After training the noise prediction network ϵ_θ , we can generate data directly from Gaussian noise: Initially, x_T is sampled from $\mathcal{N}(0, I)$. The mean and variance of the distribution $p(x_{t-1}|x_t)$ are subsequently computed according to Eq.3:

$$\mu_\theta(x_t, t) = \frac{1}{\sqrt{\alpha_t}}(x_t - \frac{\beta_t}{\sqrt{1 - \bar{\alpha}_t}}\epsilon_\theta(x_t, t)) \quad (5)$$

$$\Sigma_\theta(x_t, t) = \frac{1 - \bar{\alpha}_{t-1}}{1 - \bar{\alpha}_t}\beta_t \quad (6)$$

Therefore, x_{T-1} can be sampled from $p_\theta(x_{t-1}|x_t) = \mathcal{N}(x_{t-1}; \mu_\theta(x_t, t), \Sigma_\theta(x_t, t))$, and so on, until the predicted original image x_0 is obtained.

For a Conditional Diffusion Model(CDM) as the one in this paper, we only need to add the condition y to the noise prediction model ϵ_θ , which becomes $\epsilon_\theta(x_t, t, y)$. The pseudo-code for sampling with ResDiff is as Alg.1.

4. The Proposed ResDiff

4.1. Pre-trained CNN

To reduce additional training costs, we utilize a CNN with a reduced number of parameters to generate an initial prediction. This CNN aims to recover primary low-frequency components and partial high-frequency components, consequently facilitating the diffusion model's restoration of the more intricate high-frequency details. To ensure its generating capability, we are enlightened by [8, 11] and introduce two more loss functions (Fig.4), namely \mathcal{L}_{FFT} based on the Fast Fourier Transform (FFT) [7] and \mathcal{L}_{DWT} based on the Discrete Wavelet Transform (DWT) [29], in addition to the original loss function.

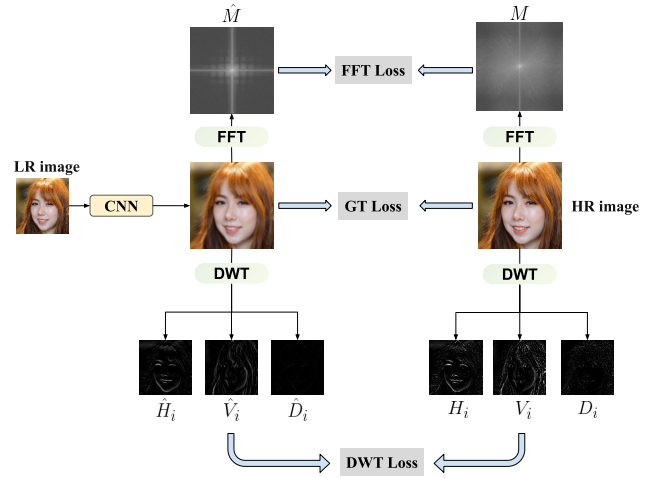


Figure 4: Depiction of the three loss functions utilized in CNN pre-training. A spatial domain loss (GT Loss) and two frequency domain losses (FFT Loss and DWT Loss) are computed.

The \mathcal{L}_{FFT} can be defined as the mean square error(MSE) between the magnitudes of the FFT coefficients of the two images:

$$\mathcal{L}_{FFT} = \mathbb{E}[\|\hat{M} - M\|^2] \quad (7)$$

where M and \hat{M} denote the frequency domain images obtained by performing FFT on the ground-truth image and the predicted image.

In a bid to enable the CNN to further recover partial high-frequency contents on top of recovering the primary low-frequency contents, we designed \mathcal{L}_{DWT} . Performing DWT on an image will decompose it into four sub-bands: low-low (LL), low-high (LH), high-low (HL), and high-high (HH). LL sub-band contains the low-frequency content of the image, while the remaining three contain the high-frequency components of the image from horizontal, vertical, and diagonal directions, respectively. The LL sub-band can perform further similar decomposition to obtain multi-layer high-frequency components. As for \mathcal{L}_{DWT} , we extract the wavelet coefficients of the high-frequency bands H , V , and D , which refer to the high-frequency components in the horizontal, vertical, and diagonal directions, respectively. For both the ground-truth image and predicted image, \mathcal{L}_{DWT} compute the MSE between each high-frequency sub-band:

$$\mathcal{L}_{DWT} = \sum_{i=1}^L \mathbb{E}[\|\hat{H}_i - H_i\|^2 + \|\hat{V}_i - V_i\|^2 + \|\hat{D}_i - D_i\|^2] \quad (8)$$

where H_i, V_i, D_i are the sub-bands of the ground-truth image in the i -th downsampling, and $\hat{H}_i, \hat{V}_i, \hat{D}_i$ are the sub-

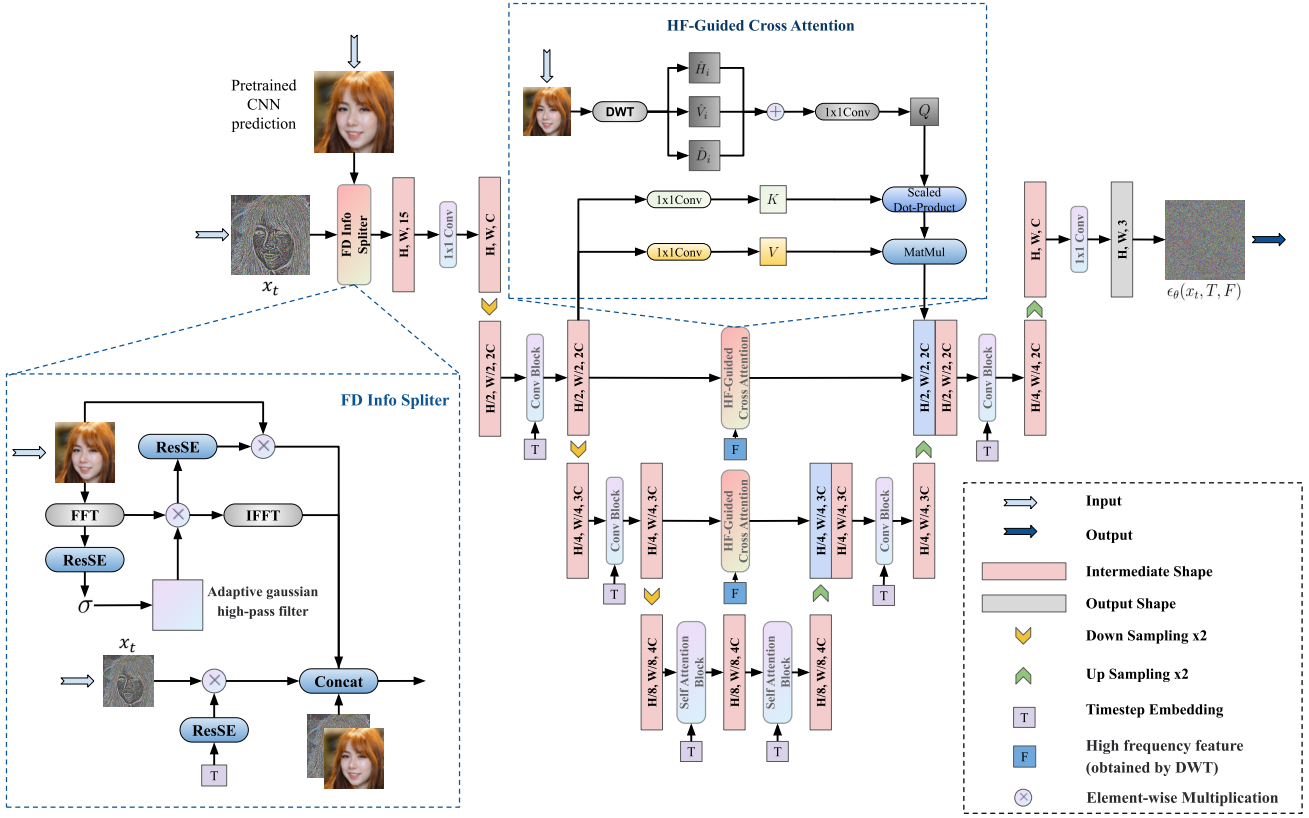


Figure 5: An overview of the model architecture in proposed FD-guided diffusion. The pre-trained CNN prediction and the noisy image x_t from step t are fed into the FD-info-Splitter, and its output is then passed on to a U-net, which is equipped with HF-guided cross-attention.

bands of the predicted image in the i -th downsampling, L is the total level of downsampling.

We also add the spatial domain loss named \mathcal{L}_{GT} : let the ground-truth image be Y , the predicted image be \hat{Y} , and \mathcal{L}_{GT} is the MSE between them:

$$\mathcal{L}_{GT} = \mathbb{E}[\|Y - \hat{Y}\|^2] \quad (9)$$

The total loss function of pre-trained CNN thus is:

$$\mathcal{L}_{CNN} = \mathcal{L}_{GT} + \alpha \mathcal{L}_{FFT} + \beta \mathcal{L}_{DWT} \quad (10)$$

where α and β are adjustable hyperparameters.

Furthermore, we design a simple CNN using residual-connection [14] and pixel-shuffle [40], named **SimpleSR**, for initial prediction (the specific structure is given in the supplementary material). Ablation studies on the proposed loss function and SimpleSR are given in the supplementary material.

4.2. FD-guided Diffusion

After obtaining the image I predicted by the pre-trained CNN, we adapt a diffusion model to predict the residuals between I and the ground truth, i.e., the high-frequency

components of the ground-truth image. To this end, we propose a Frequency-Domain guided diffusion (FD-guided diffusion), as shown in Fig.5. In contrast to SR3 [39], which simply concatenates the bilinear interpolated image with the noisy image x_t at step t , we propose a Frequency-Domain Information Splitter module (FD-Info-Splitter): I and x_t is first fed into the FD-Info-Splitter, whose output is then fed into the U-net [36]. We follow the Imagen [37], where the self-attention layer is added. In addition, a Frequency-Domain guided Cross-Attention mechanism (FD-guided CA) is designed, which utilizes the high-frequency features obtained from DWT at each layer to generate more fine-grained detail features.

4.3. FD Info Splitter

For CNN's initial prediction, low-frequency components are mixed with high-frequency contents. As the diffusion model only needs to recover high-frequency details, the input low and high-frequency features have different statuses: the former mainly assist the generation of high-frequency components globally, while the latter is required to provide guidance for fine-grained details in each region. Therefore,

we introduce Frequency-Domain Information Splitter (FD Info Splitter), which explicitly separates high-frequency and low-frequency information for better restoration. Additionally, it effectively mitigates noise for noisy images with large time steps, resulting in better noise prediction (The detailed structure of FD Info Splitter is shown in Fig.5).

For the CNN predicted images $x_{cnn} \in \mathbb{R}^{H \times W \times C}$, we first perform 2D FFT along the spatial dimensions to obtain the frequency domain feature map M :

$$M = FFT(x_{cnn}) \in \mathbb{C}^{H \times W \times C} \quad (11)$$

where $FFT(\cdot)$ denotes the 2D FFT. We adapt the methods proposed by [19, 14] and merged them into the ResSE module (Residual Squeeze-and-Excitation module), the details of which are shown in the supplementary material.

To implement adaptive high-pass filtering, a Gaussian high-pass filter is utilized whose Standard deviation is obtained from M as follows:

$$\sigma = \min(|ResSE(M)| + \frac{l}{2}, l) \quad (12)$$

where $l = \min(H, W)$. The operation for the acquired $ResSE(M)$ is for numerical stability. After obtaining σ , adaptive gaussian high-pass filter can be given directly as:

$$H(u, v) = 1 - e^{-D^2(u, v)/(2\sigma^2)} \quad (13)$$

where $D(u, v)$ is the distance from the point (u, v) in the frequency domain to the center point. The gaussian high-pass filter are then preformed element-wise multiplication with M to obtain the adaptive high-pass filtered feature map M' :

$$M' = A_{hp} \otimes M \quad (14)$$

Finally, we reverse M' back to the spatial domain by adopting inverse FFT to obtain an feature map x_{HF} rich in high-frequency components:

$$x_{HF} = FFT^{-1}(M') \in \mathbb{R}^{H \times W \times C} \quad (15)$$

where $FFT^{-1}(\cdot)$ denotes the Inverse 2D FFT. Meanwhile, we feed M' into a ResSE module to acquire the attention weights learned in the frequency domain and then perform element-wise multiplication with x_{cnn} to obtain a feature map x_{LF} containing abundant low-frequency information:

$$x_{LF} = ResSE(M) \otimes x_{cnn} \quad (16)$$

These two feature maps, dominated by high-frequency and low-frequency components, are concatenated in the channel dimension. By explicitly separating the input's mixed high-frequency and low-frequency components, the network can utilize both differently and more efficiently.

For a noisy image x_t at a large time step t , the noise components can be so large that it hinders network inference.

Hence, an adaptive denoising is utilized on x_t to obtain the partially denoised noisy image x'_t :

$$x'_t = ResSE(T) \otimes x_t \quad (17)$$

The three feature maps x_{HF} , x_{LF} , x'_t , along with x_{cnn} and x_t , are all concatenated in the channel dimension and fed into the U-net.

4.4. HF-guided CA

In the original U-net architecture, the encoder features are directly concatenated with the features obtained by the decoder [36]. This fusion facilitates the network to integrate the higher and lower-layer features effectively but lacks the ability to extract high-frequency features. To tackle this issue, we introduce a High-Frequency feature guided Cross-Attention mechanism (HF-guided CA) to recover fine-grained high-frequency details. The flow of the HF-guided CA is illustrated in Fig.5.

We utilize the pre-trained CNN prediction by extracting the \hat{H}_i , \hat{V}_i , and \hat{D}_i coefficients at the i -th level of the DWT. By adding these extracted coefficients with a linear projection, we obtain the feature map Q with aggregated high-frequency information:

$$Q = Conv_{1 \times 1}(\hat{H}_i + \hat{V}_i + \hat{D}_i) \quad (18)$$

Then, different linear projections of the input feature map M are constructed to obtain K and V in the cross-attention mechanism [18] :

$$K = Conv_{1 \times 1}(M) \quad (19)$$

$$V = Conv_{1 \times 1}(M) \quad (20)$$

The output feature map M' can then be obtained from the formula:

$$M' = Softmax\left(\frac{QK^T}{\sqrt{d_k}}\right)V \quad (21)$$

where d_k is the number of columns of matrix Q .

5. Experiments

5.1. Performance

To evaluate the performance of our ResDiff model, we compared it with previous diffusion-based and GAN-based methods using four datasets: two face datasets (FFHQ [21], and CelebA [27]) and two general datasets (Div2k [1], and Urban100 [20]). The selected evaluation metrics include two distortion-based metrics (PSNR and SSIM [46]), as well as a perceptual-based metric (FID [15]). Our ResDiff is trained solely on the provided training data to guarantee a fair comparison. The supplementary material contains detailed information about the training process, hyperparameters, and other relevant details. Since several methods did

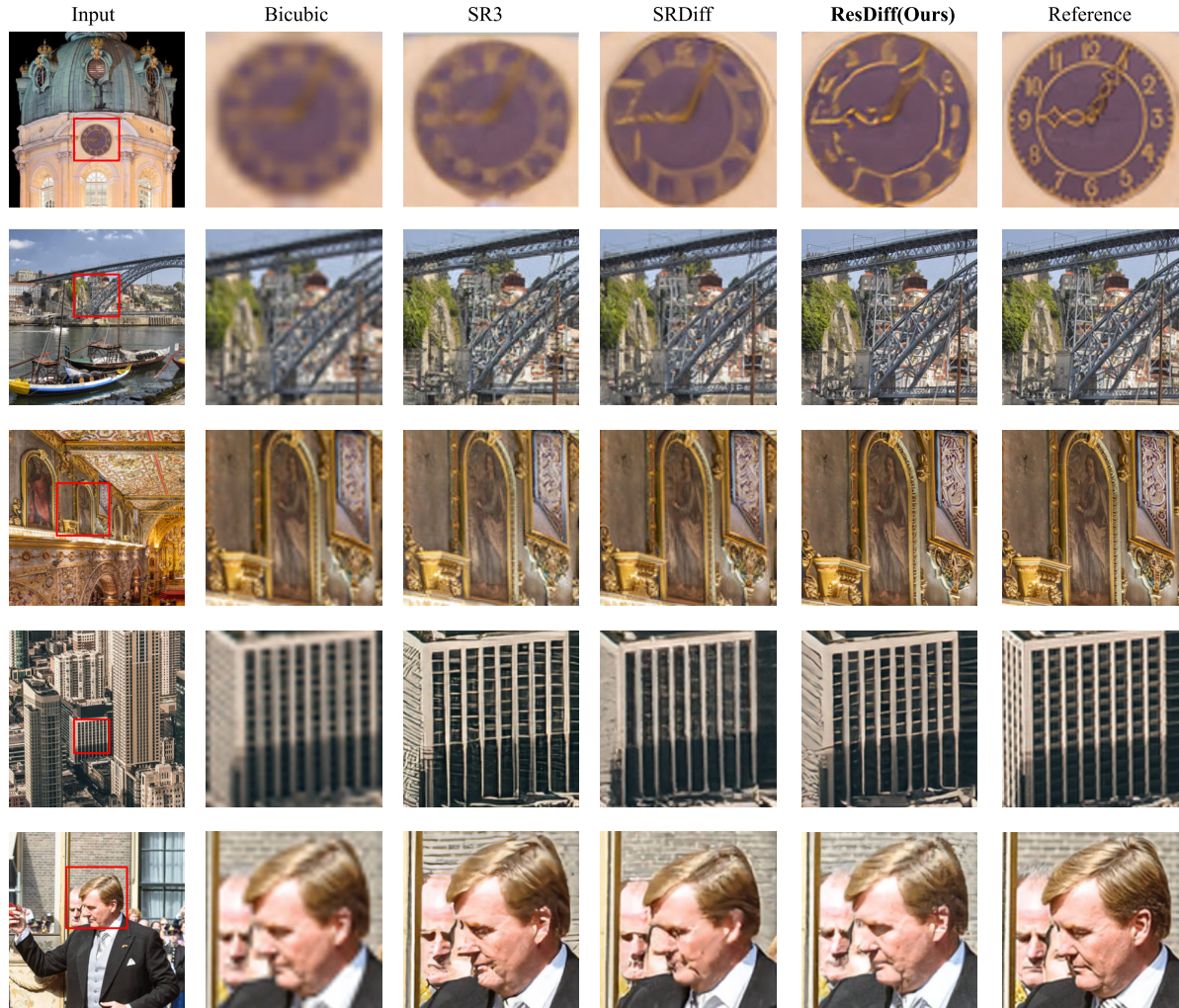


Figure 6: DIV2k 4 \times results. Note that ResDiff provides richer details and more natural textures than other diffusion-based methods for the recovery of small objects (e.g., the clock in the first column) and difficult scenes (e.g., the bridge structure in the second column, the building in the fourth column).

not state their performance on some datasets we use, their values are marked as “-” in the table. More experiments with different types of datasets are presented in the supplementary material.

FFHQ and CelebA Results The quantitative results at $32 \times 32 \rightarrow 128 \times 128$ (4 \times), $256 \times 256 \rightarrow 1024 \times 1024$ (4 \times) on FFHQ [21] and $20 \times 20 \rightarrow 160 \times 160$ (8 \times), $64 \times 64 \rightarrow 256 \times 256$ (4 \times) on CelebA [27] are shown in table 1,2. Our ResDiff demonstrates superior performance compared to all diffusion-based methods, as evidenced by the metrics presented in the table, and has about 50% reduction in Perceptual metrics (FID) than the GAN-based model.

DIV2K and Urban100 Results The quantitative results at $40 \times 40 \rightarrow 160 \times 160$ (4 \times) on DIV2K [1] and $40 \times$

$40 \rightarrow 160 \times 160$ (4 \times) on Urban100 [20] are shown in table 3. Note that ResDiff’s distortion-based metric values can significantly outperform other diffusion-based methods on these general datasets whose restoration is more difficult. Fig.6 presents partial results of ResDiff and other diffusion-based methods.

Model Convergence Speed The training curves of SR3 and ResDiff on FFHQ (4 \times) and CelebA (8 \times) are presented in Fig. 7. In subplot a, ResDiff can converge in about 250k iterations, while SR3 needs to converge in about 400k iterations. In subplot b, ResDiff also converged in about 250k iterations, while SR3 converged in about 500k. This reduction in training time and associated overhead is a major advantage of ResDiff over other diffusion-based methods.

	32 → 128			256 → 1024		
	PSNR↑	SSIM↑	FID↓	PSNR↑	SSIM↑	FID↓
Ground Truth	0.0	∞	1.000	0.0	∞	1.000
SRGAN[24]	17.57	0.688	156.07	21.49	0.515	60.67
ESRGAN[44]	15.43	0.267	166.36	19.84	0.353	72.73
BRGM[30]	24.16	0.70	-	-	-	-
PULSE[31]	15.74	0.37	-	-	-	-
SRDiff[25]	26.07	0.794	72.36	23.01	0.656	56.17
SR3[39]	25.37	0.778	75.29	22.78	0.647	60.12
ResDiff	26.73	0.818	70.54	23.15	0.668	53.23

Table 1: Quantitative comparison on the FFHQ [21] dataset, where the bolded values represent the best value in each evaluation metric.

	20 → 160			64 → 256		
	PSNR↑	SSIM↑	FID↓	PSNR↑	SSIM↑	FID↓
Ground Truth	0.0	∞	1.000	0.0	∞	1.000
ESRGAN[44]	23.24	0.66	-	-	-	-
PULSE[31]	-	-	-	22.74	0.623	40.33
SRFlow[28]	25.28	0.72	-	-	-	-
SRDiff[25]	25.32	0.73	80.98	26.84	0.792	39.16
SR3[39]	24.89	0.728	83.11	26.04	0.779	43.27
ResDiff	25.37	0.734	78.52	27.16	0.797	38.47

Table 2: Quantitative comparison on the CelebA [27] dataset, where the bolded values represent the best value in each evaluation metric.

	DIV2K 4×			Urban100 4×		
	PSNR↑	SSIM↑	FID↓	PSNR↑	SSIM↑	FID↓
Ground Truth	0.0	∞	1.000	0.0	∞	1.000
SRDiff[25]	26.87	0.69	110.32	26.49	0.79	51.37
SR3[39]	26.17	0.65	111.45	25.18	0.62	61.14
ResDiff	27.94	0.72	106.71	27.43	0.82	42.35

Table 3: Quantitative comparison on the DIV2K [1] and Urban100 [20] dataset, where the bolded values represent the best value in each evaluation metric.

5.2. Ablation Study

In this section, we perform an ablation study on FFHQ (4×) to investigate the effectiveness of each component in ResDiff, including the influence of different CNNs, and the usefulness of the proposed FD Info Splitter/HF-guided CA. The results are shown in Table 4. Note that utilizing the residual structure, even with a simple bilinear interpolation for the initial prediction, can significantly improve the performance. In terms of CNN selection, our proposed SimpleSR also outperforms SRCNN [10]. Moreover, the addition of FD Info Splitter and HF-guided CA both have an

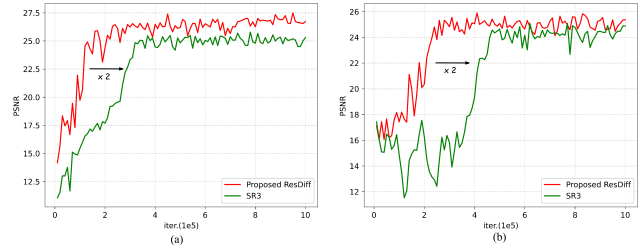


Figure 7: Curves of the PSNR of the validation set when training our ResDiff compared to SR3 [39] on FFHQ 4×SR (subplot a) and CelebA 8×SR (subplot b). ResDiff achieves convergence in almost half the time of SR3, significantly alleviating the training burden.

improvement in the results. More detailed ablation studies are given in the supplementary material.

	Model Components			Metrics		
	CNN	FD Info Splitter	HF-guided CA	PSNR↑	SSIM↑	FID↓
SimpleSR	✓	✓	✓	26.73	0.818	70.54
N/A	✓	✓	✓	25.49	0.781	74.18
Bilinear	✓	✓	✓	25.99	0.792	74.29
SRCNN[10]	✓	✓	✓	26.14	0.809	72.17
SimpleSR (only \mathcal{L}_{GT})	✓	✓	✓	26.47	0.812	71.58
SimpleSR				25.41	0.788	77.21
SimpleSR			✓	26.09	0.796	72.42
SimpleSR	✓			25.97	0.793	73.17

Table 4: Ablation study over different model components on the ffhq [21] test sets (The model components we use are placed in the first row). N/A denotes no residual structure used.

6. Conclusion and Future Work

In this paper, we propose ResDiff, a residual structure-based diffusion model. In contrast to the previous works, which only adapt LR images to generate HR images, ResDiff utilizes the feature-richer CNN prediction for guidance. Meanwhile, we introduce a frequency-domain-based loss function to the CNN and design a frequency-domain guided diffusion to facilitate the diffusion model in generating low-frequency information. Comprehensive experiments on different datasets demonstrate that the proposed ResDiff accelerates the training convergence speed and provides superior image generation quality.

Our ResDiff can also be adapted for other image restoration tasks, such as image blind super-resolution, deblurring, and inpainting. Although ResDiff can accelerate convergence, operations such as DWT are still time-consuming

and call for optimization in future work. In addition, it can be seen from the supplementary material that the color will appear a large discrepancy when the model is under-trained, which may be caused by a lack of color features in the guided high-frequency information. Utilizing a global color feature may well address this issue in future work. Moreover, our ResDiff does not outperform current State-Of-The-Art(SOTA) SISR methods [5, 49]. This is attributed to the disparity between model parameters. Due to equipment limitations, adopting a larger U-net model in ResDiff is left to future work. In addition, if a pre-trained SOTA model is applied to replace the CNN in ResDiff, it may be possible to establish a new SOTA. Finally, ResDiff may consider incorporating more DPM techniques [35, 9, 17] and superior network architectures [33, 4] in the future.

References

- [1] Eirikur Agustsson and Radu Timofte. NTIRE 2017 challenge on single image super-resolution: Dataset and study. In *2017 IEEE Conference on Computer Vision and Pattern Recognition Workshops, CVPR Workshops 2017, Honolulu, HI, USA, July 21-26, 2017*, pages 1122–1131. IEEE Computer Society, 2017. 6, 7, 8, 12
- [2] Cong Bai, Minjing Zhang, Jinglin Zhang, Jianwei Zheng, and Shengyong Chen. Lscidmr: Large-scale satellite cloud image database for meteorological research. *IEEE Transactions on Cybernetics*, 52(11):12538–12550, 2022. 12
- [3] Marco Bevilacqua, Aline Roumy, Christine Guillemot, and Marie-Line Alberi-Morel. Low-complexity single-image super-resolution based on nonnegative neighbor embedding. In Richard Bowden, John P. Collomosse, and Krystian Mikolajczyk, editors, *British Machine Vision Conference, BMVC 2012, Surrey, UK, September 3-7, 2012*, pages 1–10. BMVA Press, 2012. 12
- [4] Jieneng Chen, Yongyi Lu, Qihang Yu, Xiangde Luo, Ehsan Adeli, Yan Wang, Le Lu, Alan L. Yuille, and Yuyin Zhou. Transunet: Transformers make strong encoders for medical image segmentation. *CoRR*, abs/2102.04306, 2021. 9
- [5] Xiangyu Chen, Xintao Wang, Jiantao Zhou, and Chao Dong. Activating more pixels in image super-resolution transformer. *CoRR*, abs/2205.04437, 2022. 9
- [6] Jooyoung Choi, Sungwon Kim, Yonghyun Jeong, Youngjune Gwon, and Sungroh Yoon. ILVR: conditioning method for denoising diffusion probabilistic models. In *2021 IEEE/CVF International Conference on Computer Vision, ICCV 2021, Montreal, QC, Canada, October 10-17, 2021*, pages 14347–14356. IEEE, 2021. 1
- [7] James W. Cooley and John W. Tukey. An algorithm for the machine calculation of complex fourier series. *Mathematics of Computation*, 19:297–301, 1965. 4
- [8] Xin Deng, Ren Yang, Mai Xu, and Pier Luigi Dragotti. Wavelet domain style transfer for an effective perception-distortion tradeoff in single image super-resolution. In *2019 IEEE/CVF International Conference on Computer Vision, ICCV 2019, Seoul, Korea (South), October 27 - November 2, 2019*, pages 3076–3085. IEEE, 2019. 4
- [9] Prafulla Dhariwal and Alexander Quinn Nichol. Diffusion models beat gans on image synthesis. In Marc’Aurelio Ranzato, Alina Beygelzimer, Yann N. Dauphin, Percy Liang, and Jennifer Wortman Vaughan, editors, *Advances in Neural Information Processing Systems 34: Annual Conference on Neural Information Processing Systems 2021, NeurIPS 2021, December 6-14, 2021, virtual*, pages 8780–8794, 2021. 9
- [10] Chao Dong, Chen Change Loy, Kaiming He, and Xiaoou Tang. Learning a deep convolutional network for image super-resolution. In David J. Fleet, Tomás Pajdla, Bernt Schiele, and Tinne Tuytelaars, editors, *Computer Vision - ECCV 2014 - 13th European Conference, Zurich, Switzerland, September 6-12, 2014, Proceedings, Part IV*, volume 8692 of *Lecture Notes in Computer Science*, pages 184–199. Springer, 2014. 8
- [11] Jianfang Dou, Zimei Tu, and Xishuai Peng. Single image super-resolution reconstruction with wavelet based deep residual learning. In *2020 Chinese Control And Decision Conference (CCDC)*, pages 4270–4275, 2020. 4
- [12] Azuma Fujimoto, Toru Ogawa, Kazuyoshi Yamamoto, Yusuke Matsui, Toshihiko Yamasaki, and Kiyoharu Aizawa. Manga109 dataset and creation of metadata. *MANPU ’16*, New York, NY, USA, 2016. Association for Computing Machinery. 12
- [13] Ian J. Goodfellow, Jean Pouget-Abadie, Mehdi Mirza, Bing Xu, David Warde-Farley, Sherjil Ozair, Aaron C. Courville, and Yoshua Bengio. Generative adversarial nets. In *NIPS*, 2014. 1
- [14] Kaiming He, Xiangyu Zhang, Shaoqing Ren, and Jian Sun. Deep residual learning for image recognition. In *2016 IEEE Conference on Computer Vision and Pattern Recognition, CVPR 2016, Las Vegas, NV, USA, June 27-30, 2016*, pages 770–778. IEEE Computer Society, 2016. 5, 6, 12
- [15] Martin Heusel, Hubert Ramsauer, Thomas Unterthiner, Bernhard Nessler, and Sepp Hochreiter. Gans trained by a two time-scale update rule converge to a local nash equilibrium. In Isabelle Guyon, Ulrike von Luxburg, Samy Bengio, Hanna M. Wallach, Rob Fergus, S. V. N. Vishwanathan, and Roman Garnett, editors, *Advances in Neural Information Processing Systems 30: Annual Conference on Neural Information Processing Systems 2017, December 4-9, 2017, Long Beach, CA, USA*, pages 6626–6637, 2017. 6
- [16] Jonathan Ho, Ajay Jain, and Pieter Abbeel. Denoising diffusion probabilistic models. In Hugo Larochelle, Marc’Aurelio Ranzato, Raia Hadsell, Maria-Florina Balcan, and Hsuan-Tien Lin, editors, *Advances in Neural Information Processing Systems 33: Annual Conference on Neural Information Processing Systems 2020, NeurIPS 2020, December 6-12, 2020, virtual*, 2020. 3, 4
- [17] Jonathan Ho and Tim Salimans. Classifier-free diffusion guidance. *CoRR*, abs/2207.12598, 2022. 9
- [18] Ruibing Hou, Hong Chang, Bingpeng Ma, Shiguang Shan, and Xilin Chen. Cross attention network for few-shot classification. In Hanna M. Wallach, Hugo Larochelle, Alina Beygelzimer, Florence d’Alché-Buc, Emily B. Fox, and Roman Garnett, editors, *Advances in Neural Information Processing Systems 32: Annual Conference on Neural Information Processing Systems 2020, NeurIPS 2020, December 6-12, 2020, virtual*, pages 10230–10240, 2020. 9

tion Processing Systems 2019, NeurIPS 2019, December 8-14, 2019, Vancouver, BC, Canada, pages 4005–4016, 2019. 6

[19] Jie Hu, Li Shen, and Gang Sun. Squeeze-and-excitation networks. In *2018 IEEE Conference on Computer Vision and Pattern Recognition, CVPR 2018, Salt Lake City, UT, USA, June 18-22, 2018*, pages 7132–7141. Computer Vision Foundation / IEEE Computer Society, 2018. 6, 12

[20] Jia-Bin Huang, Abhishek Singh, and Narendra Ahuja. Single image super-resolution from transformed self-exemplars. In *IEEE Conference on Computer Vision and Pattern Recognition, CVPR 2015, Boston, MA, USA, June 7-12, 2015*, pages 5197–5206. IEEE Computer Society, 2015. 6, 7, 8, 12

[21] Tero Karras, Samuli Laine, and Timo Aila. A style-based generator architecture for generative adversarial networks. In *IEEE Conference on Computer Vision and Pattern Recognition, CVPR 2019, Long Beach, CA, USA, June 16-20, 2019*, pages 4401–4410. Computer Vision Foundation / IEEE, 2019. 6, 7, 8, 12, 13

[22] Bahjat Kawar, Michael Elad, Stefano Ermon, and Jiaming Song. Denoising diffusion restoration models. In *ICLR Workshop on Deep Generative Models for Highly Structured Data (ICLRW)*, 2022. 1

[23] Diederik P. Kingma and Jimmy Ba. Adam: A method for stochastic optimization. In Yoshua Bengio and Yann LeCun, editors, *3rd International Conference on Learning Representations, ICLR 2015, San Diego, CA, USA, May 7-9, 2015, Conference Track Proceedings*, 2015. 12

[24] Christian Ledig, Lucas Theis, Ferenc Huszar, Jose Caballero, Andrew Cunningham, Alejandro Acosta, Andrew P. Aitken, Alykhan Tejani, Johannes Totz, Zehan Wang, and Wenzhe Shi. Photo-realistic single image super-resolution using a generative adversarial network. In *2017 IEEE Conference on Computer Vision and Pattern Recognition, CVPR 2017, Honolulu, HI, USA, July 21-26, 2017*, pages 105–114. IEEE Computer Society, 2017. 2, 3, 8

[25] Haoying Li, Yifan Yang, Meng Chang, Shiqi Chen, Huajun Feng, Zhihai Xu, Qi Li, and Yueting Chen. Srdiff: Single image super-resolution with diffusion probabilistic models. *Neurocomputing*, 479:47–59, 2022. 1, 2, 3, 8, 12

[26] Jingyun Liang, Andreas Lugmayr, Kai Zhang, Martin Danelljan, Luc Van Gool, and Radu Timofte. Hierarchical conditional flow: A unified framework for image super-resolution and image rescaling. In *2021 IEEE/CVF International Conference on Computer Vision, ICCV 2021, Montreal, QC, Canada, October 10-17, 2021*, pages 4056–4065. IEEE, 2021. 2

[27] Ziwei Liu, Ping Luo, Xiaogang Wang, and Xiaou Tang. Deep learning face attributes in the wild. In *2015 IEEE International Conference on Computer Vision, ICCV 2015, Santiago, Chile, December 7-13, 2015*, pages 3730–3738. IEEE Computer Society, 2015. 6, 7, 8, 12, 16

[28] Andreas Lugmayr, Martin Danelljan, Luc Van Gool, and Radu Timofte. Srfow: Learning the super-resolution space with normalizing flow. In Andrea Vedaldi, Horst Bischof, Thomas Brox, and Jan-Michael Frahm, editors, *Computer Vision - ECCV 2020 - 16th European Conference, Glasgow, UK, August 23-28, 2020, Proceedings, Part V*, volume 12350 of *Lecture Notes in Computer Science*, pages 715–732. Springer, 2020. 2, 3, 8

[29] S. Mallat and W.L. Hwang. Singularity detection and processing with wavelets. *IEEE Transactions on Information Theory*, 38(2):617–643, 1992. 4

[30] Razvan V. Marinescu, Daniel Moyer, and Polina Golland. Bayesian image reconstruction using deep generative models. *CoRR*, abs/2012.04567, 2020. 8

[31] Sachit Menon, Alexandru Damian, Shijia Hu, Nikhil Ravi, and Cynthia Rudin. PULSE: self-supervised photo upsampling via latent space exploration of generative models. In *2020 IEEE/CVF Conference on Computer Vision and Pattern Recognition, CVPR 2020, Seattle, WA, USA, June 13-19, 2020*, pages 2434–2442. Computer Vision Foundation / IEEE, 2020. 8

[32] Kapil Mirchandani and Kushal Chordiya. Dpsrgan: Dilation patch super-resolution generative adversarial networks. In *2021 6th International Conference for Convergence in Technology (I2CT)*, pages 1–7, 2021. 2

[33] William Peebles and Saining Xie. Scalable diffusion models with transformers. *CoRR*, abs/2212.09748, 2022. 9

[34] Aditya Ramesh, Prafulla Dhariwal, Alex Nichol, Casey Chu, and Mark Chen. Hierarchical text-conditional image generation with clip latents. *ArXiv*, abs/2204.06125, 2022. 1

[35] Robin Rombach, Andreas Blattmann, Dominik Lorenz, Patrick Esser, and Björn Ommer. High-resolution image synthesis with latent diffusion models. In *IEEE/CVF Conference on Computer Vision and Pattern Recognition, CVPR 2022, New Orleans, LA, USA, June 18-24, 2022*, pages 10674–10685. IEEE, 2022. 1, 9

[36] Olaf Ronneberger, Philipp Fischer, and Thomas Brox. U-net: Convolutional networks for biomedical image segmentation. In Nassir Navab, Joachim Hornegger, William M. Wells III, and Alejandro F. Frangi, editors, *Medical Image Computing and Computer-Assisted Intervention - MICCAI 2015 - 18th International Conference Munich, Germany, October 5 - 9, 2015, Proceedings, Part III*, volume 9351 of *Lecture Notes in Computer Science*, pages 234–241. Springer, 2015. 3, 5, 6

[37] Chitwan Saharia, William Chan, Saurabh Saxena, Lala Li, Jay Whang, Emily Denton, Seyed Kamyar Seyed Ghasemipour, Burcu Karagol Ayan, S. Sara Mahdavi, Rapha Gontijo Lopes, Tim Salimans, Jonathan Ho, David J. Fleet, and Mohammad Norouzi. Photorealistic text-to-image diffusion models with deep language understanding. *CoRR*, abs/2205.11487, 2022. 1, 5, 12

[38] Chitwan Saharia, William Chan, Saurabh Saxena, Lala Li, Jay Whang, Emily L. Denton, Seyed Kamyar Seyed Ghasemipour, Burcu Karagol Ayan, Seyedeh Sara Mahdavi, Raphael Gontijo Lopes, Tim Salimans, Jonathan Ho, David J. Fleet, and Mohammad Norouzi. Photorealistic text-to-image diffusion models with deep language understanding. *ArXiv*, abs/2205.11487, 2022. 1

[39] Chitwan Saharia, Jonathan Ho, William Chan, Tim Salimans, David J. Fleet, and Mohammad Norouzi. Image super-resolution via iterative refinement. *IEEE Transactions on Pattern Analysis and Machine Intelligence*, pages 1–14, 2022. 1, 2, 3, 4, 5, 8, 12, 13

[40] Wenzhe Shi, Jose Caballero, Ferenc Huszar, Johannes Totz, Andrew P. Aitken, Rob Bishop, Daniel Rueckert, and Zehan Wang. Real-time single image and video super-resolution using an efficient sub-pixel convolutional neural network. In *2016 IEEE Conference on Computer Vision and Pattern Recognition, CVPR 2016, Las Vegas, NV, USA, June 27-30, 2016*, pages 1874–1883. IEEE Computer Society, 2016. [5](#)

[41] Jascha Sohl-Dickstein, Eric A. Weiss, Niru Maheswaranathan, and Surya Ganguli. Deep unsupervised learning using nonequilibrium thermodynamics. In Francis R. Bach and David M. Blei, editors, *Proceedings of the 32nd International Conference on Machine Learning, ICML 2015, Lille, France, 6-11 July 2015*, volume 37 of *JMLR Workshop and Conference Proceedings*, pages 2256–2265. JMLR.org, 2015. [3](#)

[42] Jiaming Song, Chenlin Meng, and Stefano Ermon. Denoising diffusion implicit models. In *9th International Conference on Learning Representations, ICLR 2021, Virtual Event, Austria, May 3-7, 2021*. OpenReview.net, 2021. [13](#)

[43] Xintao Wang, Ke Yu, Chao Dong, and Chen Change Loy. Recovering realistic texture in image super-resolution by deep spatial feature transform. In *2018 IEEE Conference on Computer Vision and Pattern Recognition, CVPR 2018, Salt Lake City, UT, USA, June 18-22, 2018*, pages 606–615. Computer Vision Foundation / IEEE Computer Society, 2018. [2](#)

[44] Xintao Wang, Ke Yu, Shixiang Wu, Jinjin Gu, Yihao Liu, Chao Dong, Yu Qiao, and Chen Change Loy. ESRGAN: enhanced super-resolution generative adversarial networks. In Laura Leal-Taixé and Stefan Roth, editors, *Computer Vision - ECCV 2018 Workshops - Munich, Germany, September 8-14, 2018, Proceedings, Part V*, volume 11133 of *Lecture Notes in Computer Science*, pages 63–79. Springer, 2018. [2, 3, 8](#)

[45] Yinhuai Wang, Jiwen Yu, and Jian Zhang. Zero-shot image restoration using denoising diffusion null-space model. In *The Eleventh International Conference on Learning Representations (ICLR)*, 2023. [1](#)

[46] Zhou Wang, Alan C. Bovik, Hamid R. Sheikh, and Eero P. Simoncelli. Image quality assessment: from error visibility to structural similarity. *IEEE Trans. Image Process.*, 13(4):600–612, 2004. [6](#)

[47] Jay Whang, Mauricio Delbracio, Hossein Talebi, Chitwan Saharia, Alexandros G. Dimakis, and Peyman Milanfar. Deblurring via stochastic refinement. In *IEEE/CVF Conference on Computer Vision and Pattern Recognition, CVPR 2022, New Orleans, LA, USA, June 18-24, 2022*, pages 16272–16282. IEEE, 2022. [1, 3, 4, 13](#)

[48] Roman Zeyde, Michael Elad, and Matan Protter. On single image scale-up using sparse-representations. In Jean-Daniel Boissonnat, Patrick Chenin, Albert Cohen, Christian Gout, Tom Lyche, Marie-Laurence Mazure, and Larry L. Schumaker, editors, *Curves and Surfaces - 7th International Conference, Avignon, France, June 24-30, 2010, Revised Selected Papers*, volume 6920 of *Lecture Notes in Computer Science*, pages 711–730. Springer, 2010. [12](#)

[49] Dafeng Zhang, Feiyu Huang, Shizhuo Liu, Xiaobing Wang, and Zhezhu Jin. Swinirf: Revisiting the swinir with fast fourier convolution and improved training for image super-resolution. *CoRR*, abs/2208.11247, 2022. [9](#)

[50] Wenlong Zhang, Yihao Liu, Chao Dong, and Yu Qiao. Ranksrgan: Generative adversarial networks with ranker for image super-resolution. In *2019 IEEE/CVF International Conference on Computer Vision, ICCV 2019, Seoul, Korea (South), October 27 - November 2, 2019*, pages 3096–3105. IEEE, 2019. [2](#)

Supplementary Material

7. Model Details

SimpleSR We designed a simple network with a few parameters named SimpleSR, which uses residual connections with the PixelShuffle module, as shown in Fig.8 (a). This network with a lesser parameter count can reduce the pre-training burden of the CNN while restoring sufficient low-frequency content.

ResSE Extracting attention weights requires global information, so simple single-layer convolution is no longer applicable while using a self-attention mechanism is too computationally expensive. Therefore, we introduce the ResSE module (Fig.8 (b)) by combining [14] and [19]. ResSE can aggregate global information with a few parameters to obtain the attention weights of feature aggregation.

8. Training Details

8.1. Datasets

For the FFHQ [21] dataset and CelebA [27] dataset, we directly downsample the HR images with a bicubic kernel. Following SrDiff [25], we select 5000 images as the test set and all other images as the training set.

For the DIV2K [1] dataset and Urban100 [20] dataset, we crop the HR images into 160×160 patches and downsample with the bicubic kernel sequentially in the training phase, just like SrDiff. In the testing phase, we downsample the original HR images and get the SR prediction images based on the LR images. The DIV2K test set uses its given test set of 100 images, and for Urban100, we select 20 images as the test set (such a smaller test set may affect the calculation of FID metrics).

8.2. Model and Training Configuration

We set the initial number of Channels in U-net to 64, with channel multipliers 1, 2, 4, 8, 8. The self-attention blocks [37] are only added to the bottom and penultimate layers, and two residual convolution blocks [14] are used in each Conv block, with the dropout set to 0.2.

For the training of the diffusion model, we used the Adam [23] optimizer with a learning rate set to 1×10^{-4} and a batch size set to 4. The total time step T was set to 1000, using a linear increase in $\beta_{1:T}$ from 1×10^{-6} to 1×10^{-2} . We trained on 1 NVIDIA Tesla A100 with 100k steps.

For CNN pre-training, we performed only 10k iterations and set the batch size to 128 due to the small size of the network. The rest of the hyperparameters were kept the same as above.

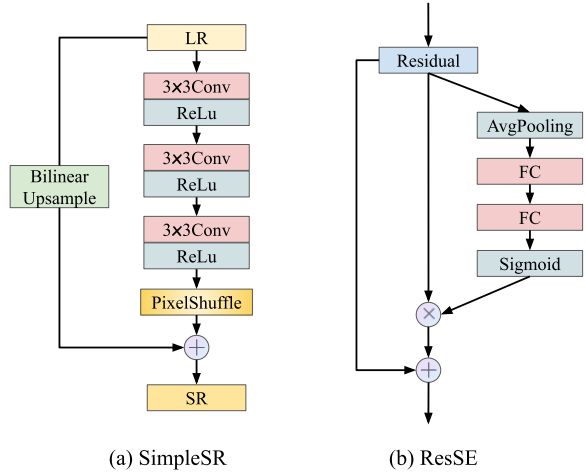


Figure 8: Network architecture of SimpleSR and ResSE.

9. Additional Experimental Results

9.1. Additional Dataset Results

	LSCIDMR 4×		Manga109 4×	
	PSNR↑	SSIM↑	PSNR↑	SSIM↑
Ground Truth	∞	1.0	∞	1.0
SRDiff[25]	27.54	0.807	27.04	0.813
SR3[39]	26.13	0.782	26.88	0.805
ResDiff	27.79	0.812	27.76	0.832

Table 5: Quantitative comparison on the LSCIDMR [2] and Manga109 [12] dataset, where the bolded values represent the best value in each evaluation metric.

	Set5 4×		Set14 4×	
	PSNR↑	SSIM↑	PSNR↑	SSIM↑
Ground Truth	∞	1.0	∞	1.0
SRDiff[25]	28.72	0.843	25.63	0.702
SR3[39]	27.31	0.767	25.29	0.684
ResDiff	29.32	0.854	26.19	0.718

Table 6: Quantitative comparison on the Set5 [3] and Set14 [48] dataset, where the bolded values represent the best value in each evaluation metric.

To verify the generalizability of the model, we performed the same comparison of each diffusion-based method on LSCIDMR (a satellite cloud image dataset) [2] and Manga109 (comic image dataset) [12]. Fig.9 presents the results of ResDiff on the LSCIDMR dataset (4×). Furthermore, we use the weights trained on the DIV2k [1] dataset to test on the set5 [3] and set14 [48] dataset. The

results are shown in Table 5, 6. Note that the proposed ResDiff can still outperform other diffusion-based methods. Fig.10 presents the results of different diffusion-based methods on the set14 dataset (4 \times).

9.2. Additional Ablation Study

Hyperparameters		Metrics			
Total Time Step	Channel Size	Loss	PSNR \uparrow	SSIM \uparrow	FID \downarrow
1000	64	l_1	26.73	0.818	70.54
50	64	l_1	25.54	0.772	76.89
200	64	l_1	25.93	0.795	74.54
2000	64	l_1	26.84	0.818	68.70
50 \dagger	64	l_1	26.28	0.812	72.38
1000	32	l_1	26.41	0.809	74.26
1000	128	l_1	26.78	0.821	71.06
1000	64	l_2	26.36	0.804	74.73

Table 7: Ablation study over different hyperparameters on the ffhq [21] test sets (The hyperparameters we use are placed in the first row). Where the \dagger denotes using DDIM [42] sampling.

We explore the effects of hyperparameters as different total time-step T , channel size c in U-net and choose L_1 loss or L_2 loss. These ablation experiments are also performed on the FFHQ dataset ($32 \times 32 \rightarrow 128 \times 128$), and the results are shown in Table 7. It can be seen that the longer the total time step, the better the model performance, but the correspondingly lower the sampling speed. In addition, the number of channels in the U-net is underfitting at a low number (32) and overfitting at a high number (128). Finally, it can be found that l_2 loss is inferior to l_1 loss, consistent with [47, 39].

9.3. Additional Sampling Results

Fig.11 illustrates the image colour deviation of ResDiff when the convergence is not completed, a problem caused by not aggregating the colour information effectively. Fig.12 presents the diffusion iterations on the DIV2K dataset, and Fig.13 demonstrates more high-resolution images of ResDiff sampled on the FFHQ (4 \times) and DIV2K (4 \times) datasets.

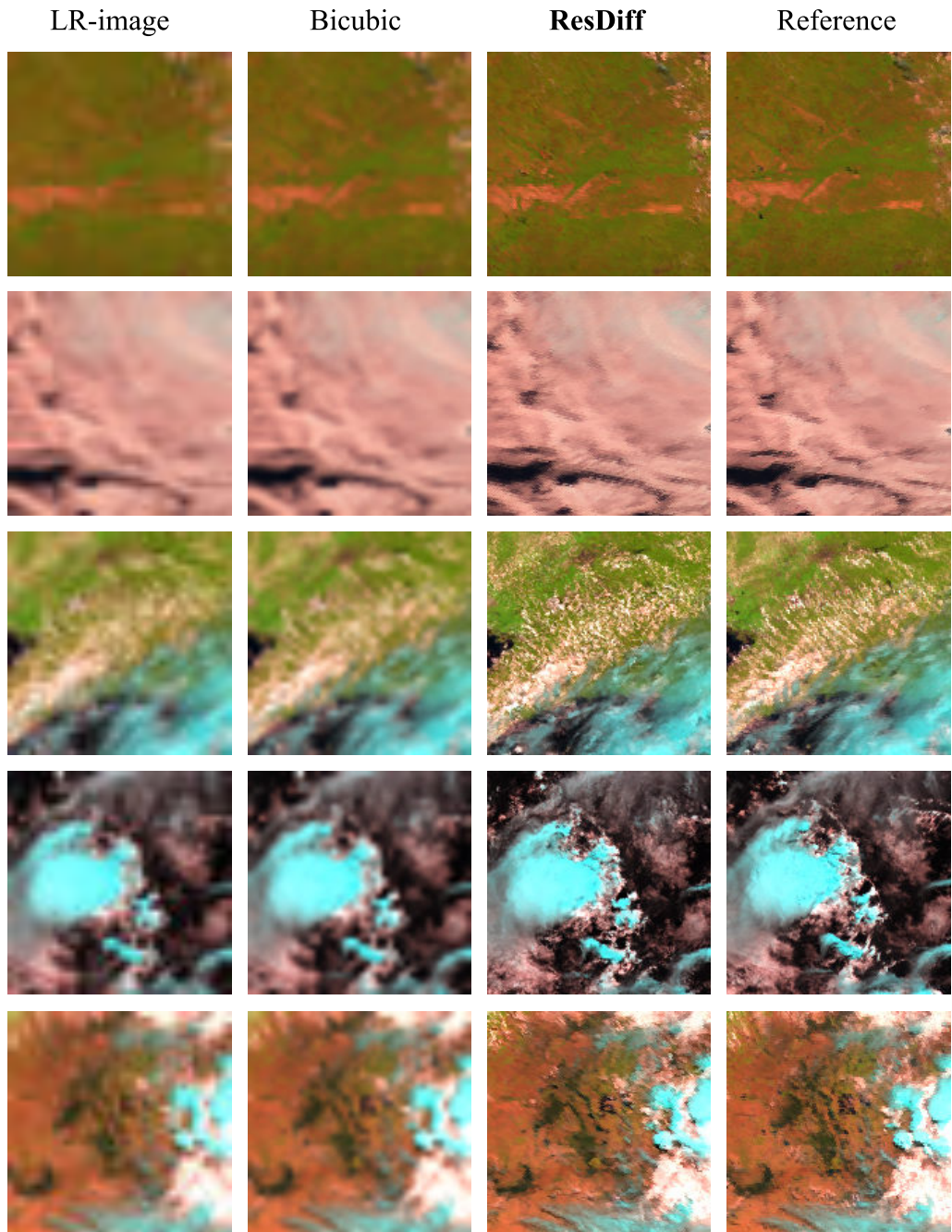


Figure 9: LSCIDMR $4\times$ results. The image super-resolution of remote-sensing dataset demands the restoration of more texture details, and ResDiff accomplishes this well.

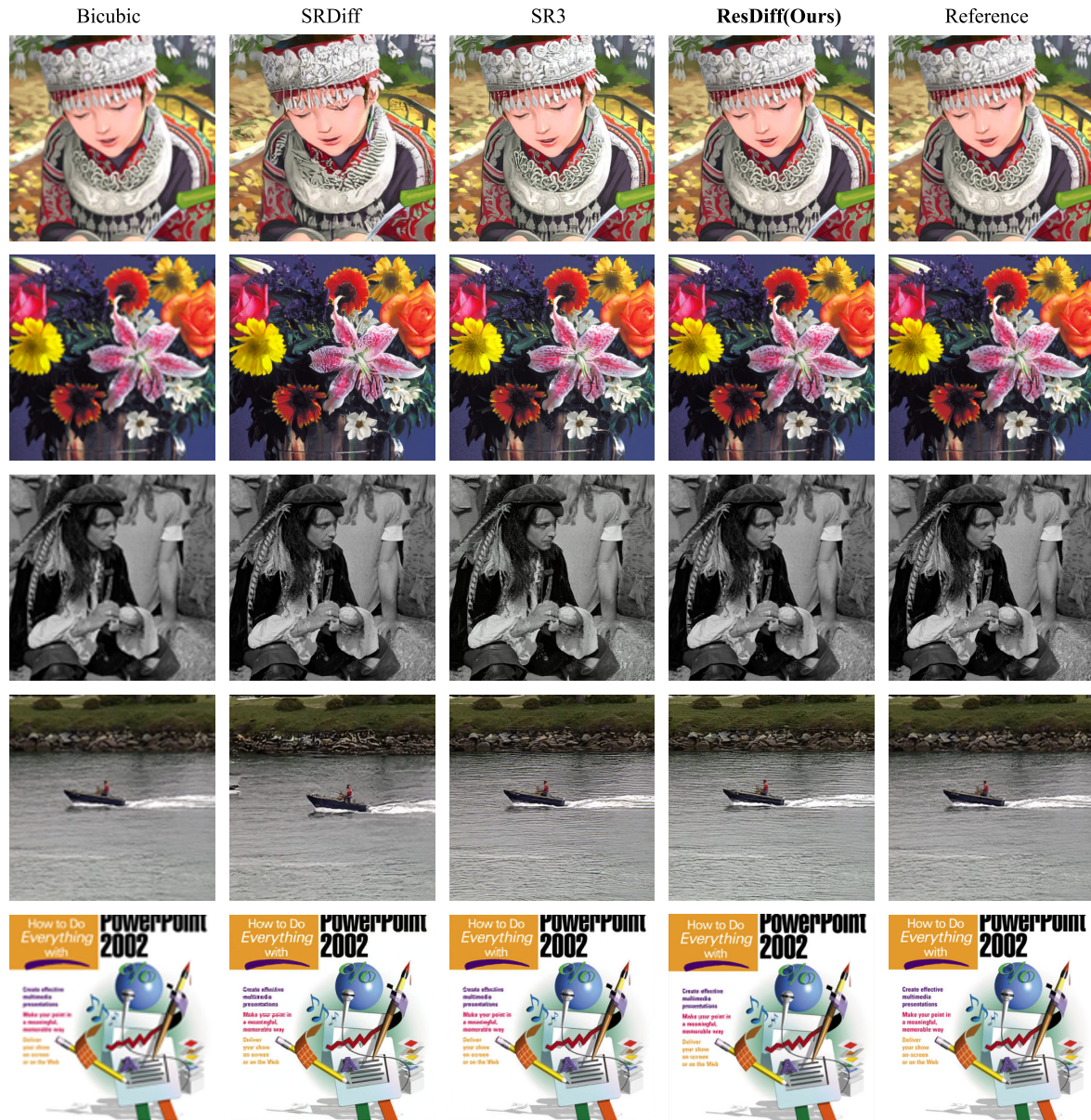


Figure 10: Set14 4× results. Compared to other diffusion-based methods, ResDiff generates images with richer textures and sharper edges.

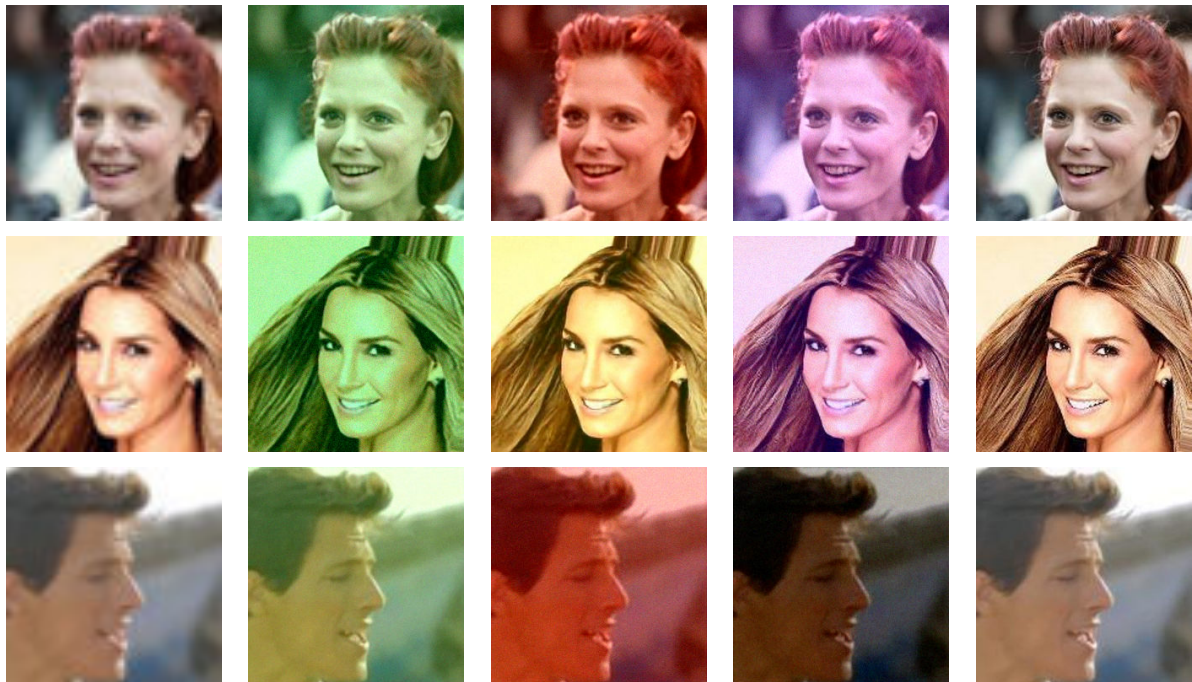


Figure 11: Demonstration of image colour deviation problems on CelebA [27] (4×). The leftmost image is the LR image, the rightmost image is the HR image, and the middle is the predicted image when the model has not converged. Note that although the model has been able to learn satisfactory margin information, there is a significant colour difference.

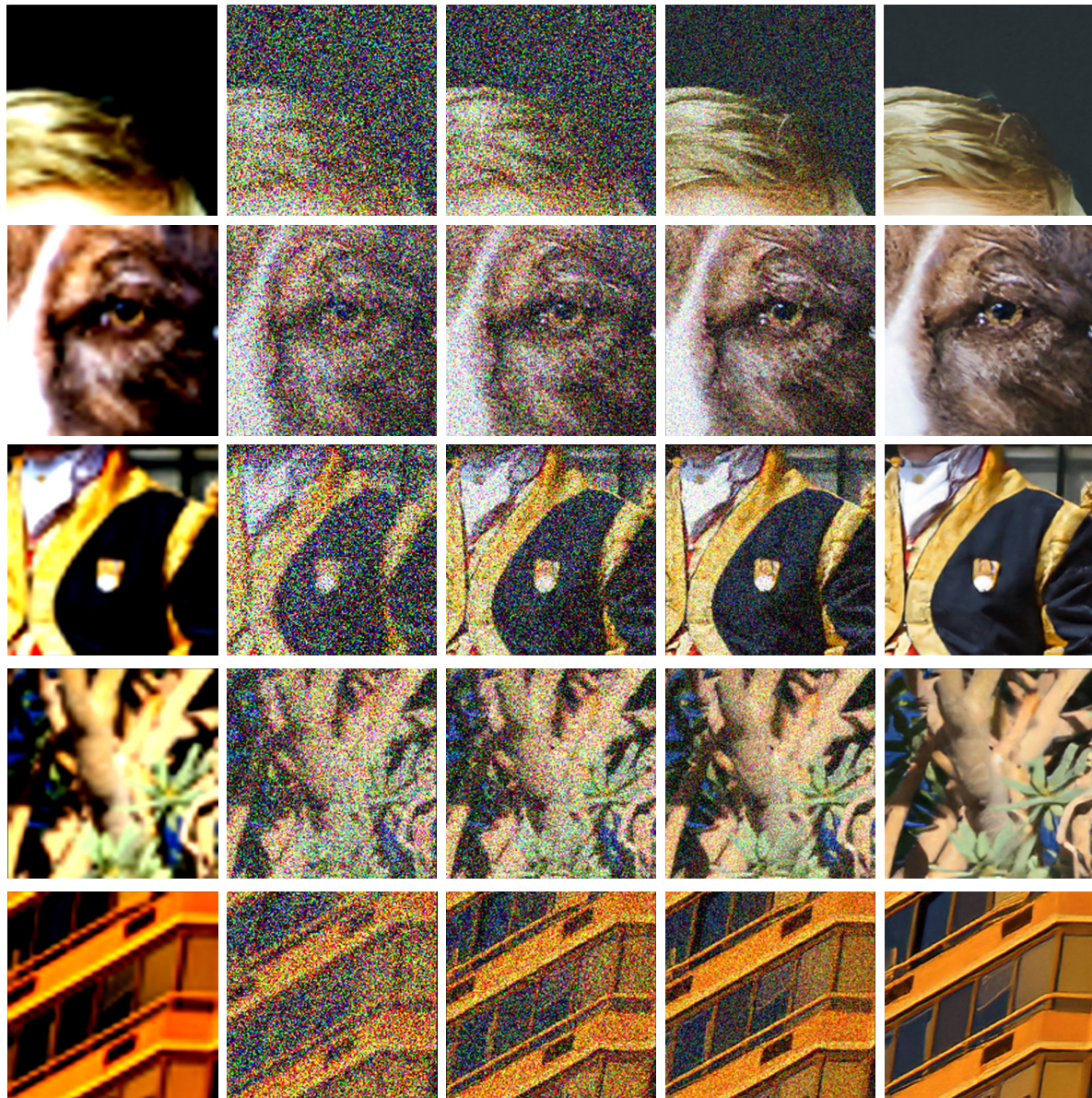


Figure 12: The diffusion process of ResDiff on the DIV2K dataset. The leftmost image shows the initial prediction of the CNN, and the following four images show the denoising process of the image in turn.



Figure 13: Partially sampled high-resolution images from ResDiff on the DIV2K dataset (4 \times).